

The combustion of *iso*-octane droplets with initial diameters from 0.5 to 5 mm: Effects on burning rate and flame extinction

Yuhao Xu^a, Michael C. Hicks^b, C. Thomas Avedisian^{a,*}

^a Sibley School of Mechanical and Aerospace Engineering, Cornell University, Ithaca, NY 14853, USA

^b NASA Glenn Research Center, Combustion and Reacting Systems Branch, Cleveland, OH 44135, USA

Received 3 December 2015; accepted 24 July 2016

Available online 8 October 2016

Abstract

The burning characteristics of *iso*-octane droplets in the standard atmosphere are reported over a large range of initial droplet diameters ($0.5 \text{ mm} < D_o < 5 \text{ mm}$) for near one-dimensional droplet flames as promoted by low gravity. A ground-based drop tower and a space-based platform (International Space Station) were used to provide an environment to examine the influence of D_o that encompasses regimes where radiation does not have an effect on burning to where it does. For $D_o < 2.7 \text{ mm}$, the droplets burned to completion without extinction. Larger droplets evidenced extinction due to radiative emissions from the flames to the ambience that produced a two stage burning process. The burning rate (K) was nearly constant in the first stage and then gradually decreased. Concurrently, radiation emissions dropped by two orders of magnitude and ‘flickering’ flames were noted during the transition. After extinction, burning entered a regime where K gradually decreased with time and approached values commensurate with evaporation in a heated environment (i.e., no combustion). Energy balances based on scale analyses related K and flame temperature (T_f) to D_o : a balance at the flame including radiation losses led to the scaling $K \sim D_o^{-n}$ in reasonable agreement with the data for $D_o > 2 \text{ mm}$; an energy balance at the droplet surface showed that T_f quickly dropped from $\sim 1600 \text{ K}$ to $\sim 700 \text{ K}$ after flame extinction, followed by a gradual reduction of T_f to near ambient temperature. The trends in the data are also discussed for potentially revealing a possible low temperature combustion regime.

© 2016 Published by Elsevier Inc. on behalf of The Combustion Institute.

Keywords: Droplet combustion; Spherical symmetry; Microgravity; *iso*-Octane; Surrogate fuel

1. Introduction

iso-Octane (2,2,4-trimethylpentane) has long been considered a component of “primary reference fuels” (PRFs) [1,2]. It is a branched component of gasoline and jet fuel [3,4], and *iso*-octane

* Corresponding author.

E-mail address: cta2@cornell.edu (C.T. Avedisian).

has also been included as a surrogate component for other transportation fuels [5]. Many studies have reported on its combustion performance including full-scale engine tests to assess end-use performance [6,7]¹ and fundamental studies that have developed and validated *iso*-octane's combustion chemistry [8–11] using experimental configurations that emphasize “combustion kinetic phenomenon” [5]. These configurations share the common element of being amenable to detailed numerical modeling (DNM) [12], which is a necessary capability for evaluating combustion chemistry and property data inputs for surrogates.

A combustion configuration for a liquid fuel that combines evaporation and combustion is that of an isolated droplet burning with spherical symmetry. It incorporates many elements that arise in sprays [13] including moving boundary effects, transient transport processes, combustion chemistry, soot formation, and radiative transport dynamics. Spherically symmetric droplet burning is also amenable to DNM [14–18]. Data obtained for this configuration have significant values for assessing the efficacy of combustion chemistry and property data inputs of the burning process.

Few studies have examined the burning characteristics of *iso*-octane droplets under conditions that would ostensibly promote spherical symmetry. The early work of Faeth and Olson [19] is notable for their study of ignition delay in conditions that promote spherical symmetry applicable to a theoretical analysis. Droplets burning in a low gravity environment were examined by carrying out the experiments in a 4.8 m drop tower using the fiber supported method. For the range of initial droplet diameter (D_o) examined, $700\ \mu\text{m} < D_o < 1800\ \mu\text{m}$, a fiber diameter of $200\ \mu\text{m}$ with a $500\ \mu\text{m}$ bead at the tip would likely have resulted in an influence of the fiber on the burning process through various thermal effects [20,21]. A much later study of *iso*-octane droplets [3] examined the influence of mixture fractions for *iso*-octane/*n*-heptane blends for $D_o \approx 0.5\ \text{mm}$. The results showed that *iso*-octane and *n*-heptane had almost identical burning rates (K) and that *iso*-octane flames were slightly closer to the droplet than *n*-heptane flames. For the relatively small droplets employed, radiation effects were unlikely to influence the burning process [22–24].

Recent DNM and experimental studies of spherically symmetric droplet burning have illustrated the influence of radiation for droplets typically larger than about 2 mm for *n*-heptane, *n*-octane and *n*-decane burning in the standard atmo-

sphere. Flame extinction and in some cases, transitions to burning regimes characterized by low temperature combustion (LTC) chemistry were found [17,18,25–28].

The present study examines experimentally the influence of D_o on *iso*-octane droplets burning in the standard atmosphere over the range of $0.5\ \text{mm} < D_o < 5\ \text{mm}$. The purpose is to examine how the combustion process of *iso*-octane droplets responds to varying D_o over such a wide range, in particular the burning rate, flame extinction and transitions to combustion regimes that would potentially be strongly influenced by radiative effects. In addition, a scaling approach based on energy balances at the droplet and flame is used to explain the observed trends.

2. Experimental methods

The experimental designs create droplets that are ostensibly stationary in a stagnant ambient in a low gravity ($\sim 10^{-4}$ of Earth's normal gravity) environment to promote spherically symmetric droplet flames. Both ground-based (GB, $D_o < 0.8\ \text{mm}$ [3]) and space-based International Space Station (ISS, $0.90\ \text{mm} < D_o < 5\ \text{mm}$) platforms are used to access the desired range of D_o . The ambient is room temperature air at atmospheric pressure. A brief description of each experimental design is given below.

Small droplets are studied in a ground-based drop tower [3,21,29] that provides a 7.6 m free-fall distance ($\sim 1.2\ \text{s}$ of experimental time (t)) within which the experiments are performed. Test droplets are deployed onto two small ($14\ \mu\text{m}$ diameter) SiC fibers using a piezoelectric generator. Once the fuel droplet is positioned at the intersection of the two fibers, the instrumentation package within which the deployment hardware and cameras are mounted is released into free-fall to initiate the low gravity period. A drag shield is employed to achieve the desired low gravity level during free-fall for the GB experiments. The effects of the fibers for the experimental design employed here were discussed previously and shown not to influence K or flame diameter [21,29].

Droplets are ignited 320 ms after initiating the fall by activating two sparks across two pairs of electrodes positioned on opposite sides of the droplet for $800\ \mu\text{s}$. The electrodes are retracted immediately after ignition to minimize the influence on the thermal field around the droplet during its combustion. The burning process is recorded by two cameras that give perpendicular views of the droplet during combustion (a black and white (BW) digital camera (Canadian Photonics Labs, Inc., MS-80K, 3.9 megapixels (MP)/frame, operated at 200 fps) records the back-lit droplet and soot shell with backlighting provided by a 1-W LED lamp (Black Diamond Equipment, LTD); a

¹ The cited papers on engine tests are representative of some of the literature concerning *iso*-octane combustion. They are not meant to be a complete listing. Other citations in the following discussions are similarly selective due to space limitations.

color camera (Hitachi HV-C20, 0.3 MP/frame, operated at 30 fps) records self-illuminated droplet flames).

For large droplets ($0.90 \text{ mm} < D_o < 5 \text{ mm}$), the Multi-user Droplet Combustion Apparatus (MDCA) onboard the ISS is used to perform the experiments. Detailed hardware descriptions are reported elsewhere [30–32]. For the large droplet experiments reported here, only free-floating droplets are studied.

Droplets within the MDCA are formed by dispensing liquid fuel through two needles which are separated by a small distance to create a liquid bridge. Once the desired droplet size is reached, the liquid bridge is slightly stretched to minimize drift after droplet deployment. The needles are then rapidly retracted leaving behind a free droplet. The droplet is then ignited by two Kanthal wire loops that are energized and retracted after ignition. Note that ignition energy is expected to be dependent in part on D_o . In the reported experiments, the minimum ignition energy is employed for each D_o investigated. Moreover, ignition disturbances, if they exist, typically dissipate within the first 10% of the burning history as shown in Ref. [3] and exert no influence thereafter.

For the MDCA experiments, the droplet burning process is recorded by a High Bit-Depth Multispectral camera (1 MP at 30 fps) with a back-light source for droplet and soot images and a color camera (0.3 MP at 30 fps) for flame images. The hardware also includes two radiometers with a sampling frequency of 100 Hz: one covering wavelengths ranging between 0.1 and $54 \mu\text{m}$ (which is encapsulated with Argon gas and sealed within a KrS-5 (i.e., Thallium Bromide) window); and the other being narrowband, encapsulated with Xenon gas, that uses a filter made by overlaying a $5\text{-}\mu\text{m}$ “long-wave pass” fused quartz (i.e., SiO_2) window over a sapphire (i.e., Al_2O_3) window with a transmission cut-off at $7.145 \mu\text{m}$ and a full width at half maximum of $1.54 \mu\text{m}$. The wideband and narrowband radiometers are optimized to be sensitive to the hot flame and LTC, respectively.

The *iso*-octane used in the experiments is purchased from Sigma-Aldrich with a purity of 99.8%. Representative properties are given in Table 1.

Table 1
Selected properties of *iso*-octane.

Formula	C_8H_{18}
Stoichiometric coefficient ν	12.5
Molecular weight (g/mole) [33]	114.29
Boiling point T_b (K) [33]	372.35
Liquid density ρ_L (@ T_b , kg/m^3) [3]	637.90
Heat of vaporization (@ T_b , kJ/kg) [33]	269.4
Cetane number [12]	15
Lower heating value (MJ/kg) [9]	44.31
Adiabatic flame temperature (K) [34]	2233.3

Video images recorded by BW and color cameras provide the main diagnostic for the experiment in the present study. The video images are processed either by an automated algorithm [35] or manually using a commercial software package (Image-Pro Plus v6.3). The manual approach involves positioning a virtual ellipse around the boundary of the droplet, soot shell, or flame. The equivalent diameter is then obtained as $(H \times W)^{0.5}$, where H and W are major and minor axes of the ellipse, respectively. The manual measurement approach is always adopted for soot shell (D_s) and flame (D_f) diameter extractions, where the outer boundary of the blue luminous zone defines the flame boundary. For the data reported here, approximately 11,000 data extraction operations are performed.

Measurement uncertainty arises from two sources: repeatability from run-to-run and the precision by which measurements can be extracted from images (i.e., image analysis). Regarding the former, ‘average’ and ‘standard deviations’ of measurements are obtained by repeating experiments under identical conditions. However, ISS test operations typically involve sweeping through a range of conditions (here being D_o) rather than holding conditions fixed and repeating experiments. As such, it is impossible to obtain meaningful averages and standard deviations of ISS droplet data. On the other hand, the main source of measurement error arises from identifying the boundary thickness of the droplet, soot shell, and flame, consisting of approximately 3, 15, and 5 pixels, respectively. As such, the measurement precision of data extraction operations from video images for droplet diameter (D), D_s , and D_f ranges from $\pm 2.0\%$ to $\pm 11.5\%$, $\pm 4.8\%$ to $\pm 18.8\%$, and $\pm 2.6\%$ to $\pm 10.0\%$, respectively.

3. Results and discussions

Figure 1 shows selected color and BW images from both GB and ISS experiments (separated by the vertical dashed line). The needle-like glows on either side of GB droplet flames are the result of interactions between the flame and fiber. The images are cropped and centered to the droplet (in reality the ISS droplets move somewhat due to the deployment process).

The flame color in Fig. 1a arises from incandescence of soot particles, formed on the fuel-rich side of the flame, that pass through the flame and burn in the reaction zone. Based on the flame temperature that exists, the resulting yellow glow of the droplet diffusion flame is due to the collective wavelength of the soot incandescence and the sensitivity of the imaging optics to the visible spectrum. Without soot, the dominant flame color is blue due to CH radicals that emit in the blue region of the spectrum. Note that the blue flame is not caused by the deficient diffusion of oxygen in the apparatus since

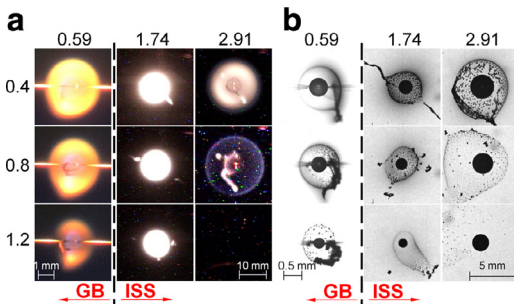


Fig. 1. Selected color (a) and BW (b) images from GB and ISS *iso*-octane experiments. Numbers on top represent D_o (mm) and vertically are normalized time (s/mm^2). Flame color transitions from yellow to blue for $D_o = 2.91$ mm. Indicated scales for GB and ISS photographs are different. Image 2.91:0.8 in 'a' is contrast-enhanced to better show the flame.

the volume of the droplet flame is only a tiny portion ($\sim 0.014\%$ maximum) of the MDCA chamber volume.

The flame intensity (Fig. 1a) qualitatively decreases with increasing D_o and a flame extinction process is clearly revealed (2.91:0.4 to 2.91:1.2) by disappearance of the visible flame. No such process is observed in any of the GB experiments. Instead, the GB droplet flames first expand then grow progressively dimmer and disappear with burnout. Figure 1b shows selected BW images that highlight the sooting dynamics. The soot shell is more intact and spherical throughout the burning history for the GB droplets because their motion is restricted by the support fiber. The unsupported ISS droplets are allowed to drift about in the combustion chamber. Drifting can affect the shape of the soot shell as shown in Fig. 1b. However, the velocities of such drifting are too low to influence K based on standard convective corrections.

The evolution of droplet diameter for selected experimental runs in scaled coordinates is shown in Fig. 2 (data from all runs are provided in the Supplementary Materials Section).

Two broad regimes are shown: an initial regime for $D_o < 2.7$ mm where the evolution of scaled diameter is linear until burnout (some data are not shown for clarity) and the burning rate ($K \equiv \left| \frac{d(D/D_o)}{d(t/D_o^2)} \right|$) is essentially constant; and a second regime for larger droplets ($D_o > 2.7$ mm) where K decreases (the tail-off effect shown in Fig. 2), which coincides with disappearance of the visible flame (cf. 2.91:0.8 and 2.91:1.2 in Fig. 1a). We believe these trends are due to radiative losses that are absent in the small droplets examined (taking the cutoff for radiation at about $D_o \sim 1$ mm [23]) but present in the large droplets.

In the first regime the trends in Fig. 2 do not show extinction-like effects and the droplet

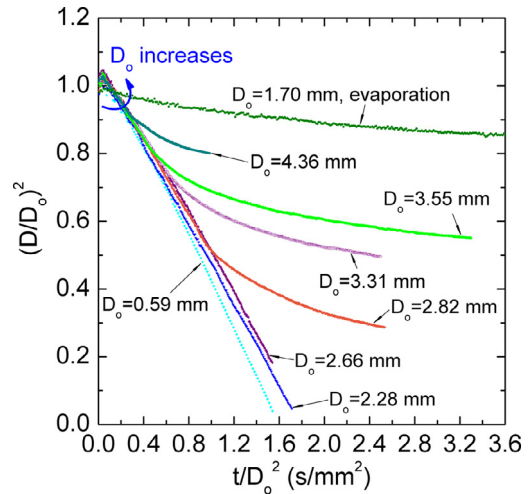


Fig. 2. Evolution of droplet diameter for *iso*-octane for selected D_o .

flames are visible throughout burning. In the second, post-extinction regime, K decreases considerably and ultimately achieves a value commensurate with evaporation (i.e., no combustion). The data labeled 'evaporation' is shown for reference, though at a different D_o . However, the trends of the post-extinction data in Fig. 2 suggest convergence to the same asymptotic evaporation rate. Two extinction mechanisms to consider are radiative and diffusive (in the sense of fuel leakage through the flame). The potential for a fuel leakage extinction mechanism can be assessed by examining the product of $D_{ext}K$ (where D_{ext} is extinction diameter), which should be constant [36]. To estimate K we take an average value (i.e., $K = K_{avg}$), obtained by linearizing the measurements (Fig. 2) in the pre-extinction regime and Fig. 3a shows the results. Though the data in Fig. 2 exhibit a slight variation with time (most likely due to droplet heating effects that persist throughout burning [29]) and we do use this time variation later to estimate the evolution of flame temperature (T_f), it is sufficient here to use a single average value to determine $D_{ext}K_{avg}$. Figure 3b shows that $D_{ext}K_{avg}$ strongly depends on D_o . As such, it is unlikely that diffusive and fuel leakage effects will characterize the extinction mechanism for the data reported here.

The relative positions of the flame to the droplet (flame standoff ratio, $FSR = D_f/D$) and the soot shell to the droplet (soot standoff ratio, $SSR = D_s/D$) for data corresponding to $D_o > 1$ mm are shown in Fig. 4. As expected, $SSR < FSR$ because soot forms on the fuel-rich side of the flame. The SSR appears to increase slightly with increasing D_o though the trend is not significant. An explanation is uncertain as it involves a balance of the forces acting on the aggregates [37] which depend

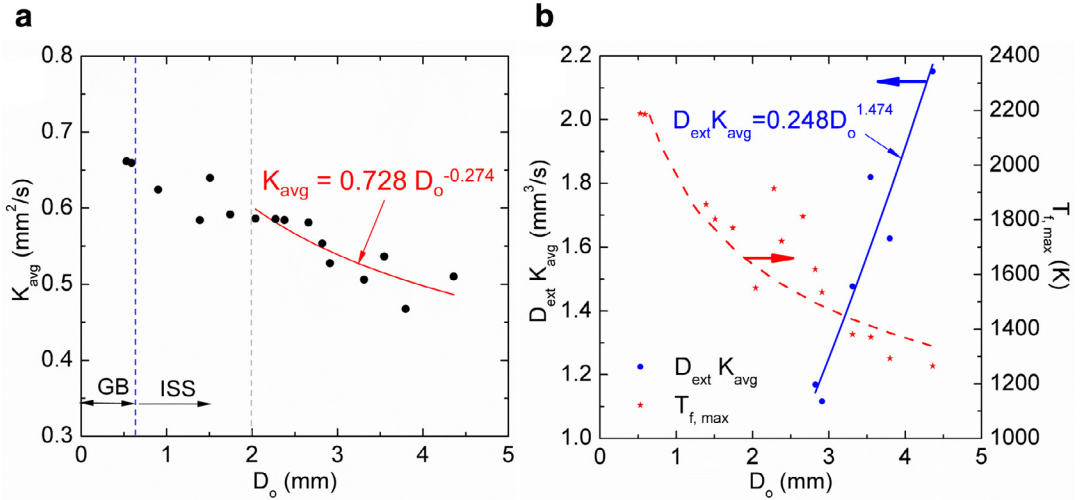


Fig. 3. (a) Dependence of K_{avg} obtained from the most linear portion of the burning history on D_o where the correlation equation is valid for $D_o > 2$ mm; (b) variation of $D_{ext}K_{avg}$ and ‘maximum’ flame temperature ($T_{f,max}$) with D_o .

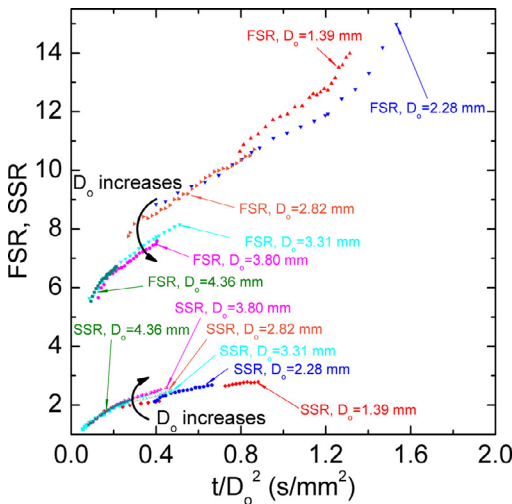


Fig. 4. Evolution of flame and soot standoff ratios for *iso*-octane investigated in this study. Results presented here are for selected test runs where radiation effects are important during the burning history.

not only on the temperature gradient and hence T_f but also K and other properties.

For a given D_o , the variation of FSR with time shown in Fig. 4 is typical [3,15,16] whereby the flame moves away from the droplet as burning proceeds. This trend contrasts with the classical theory of burning [38] which leads to the FSR being constant.

As shown in Fig. 4 the FSR decreases with increasing D_o . As D_o increases, radiation to the surrounding increases as well so that the flame has to

move closer to the droplet to sustain fuel evaporation that maintains burning. The flame temperature (T_f) should figure prominently in this process as it is expected to be strongly dependent on D_o . We do not have a direct numerical model of the droplet burning process for *iso*-octane that would allow establishing the relationship between T_f and variables. A simple estimate for T_f can, though, be obtained with the aid of scale analysis of an energy balance at the droplet surface that equates the energy to evaporate the fuel with the energy conducted to the droplet (neglecting radiation in the inner region between the droplet and flame). The result shows that [26]

$$T_f \sim T_b + \frac{\rho_L h_{fg} K}{8k_p} \left(\frac{D_f}{D} - 1 \right) \quad (1)$$

where T_b , ρ_L , h_{fg} , and k_p , are fuel boiling point, liquid density, latent heat of vaporization, and gas thermal conductivity, respectively.

To evaluate T_f for purposes of explaining the influence of D_o on D_f/D , we will estimate a ‘maximum’ flame temperature, $T_{f,max}$, to correspond to the highest flame standoff ratio and burning rate, and assume $K = K_{avg}$ in Eq. (1). For D_f/D , we use the value just prior to burnout or extinction (i.e., last data entry for the indicated D_o in Fig. 4 which gives the highest D_f/D value). The liquid density and heat of vaporization in Eq. (1) are evaluated at T_b , k_p is evaluated at $T_p = (T_f + T_b)/2$ [38] (so $T_{f,max}$ is determined iteratively from Eq. (1)) with $k_p = 0.4k_{i-O} + 0.6k_{air}$ (where k_{i-O} and k_{air} are thermal conductivity of *iso*-octane and air, respectively), assuming a fuel mole fraction $\chi = 0.4$ [39]; k_{i-O} is obtained using the Roy/Thodos method suggested by Reid et al. [40], and k_{air} is computed from

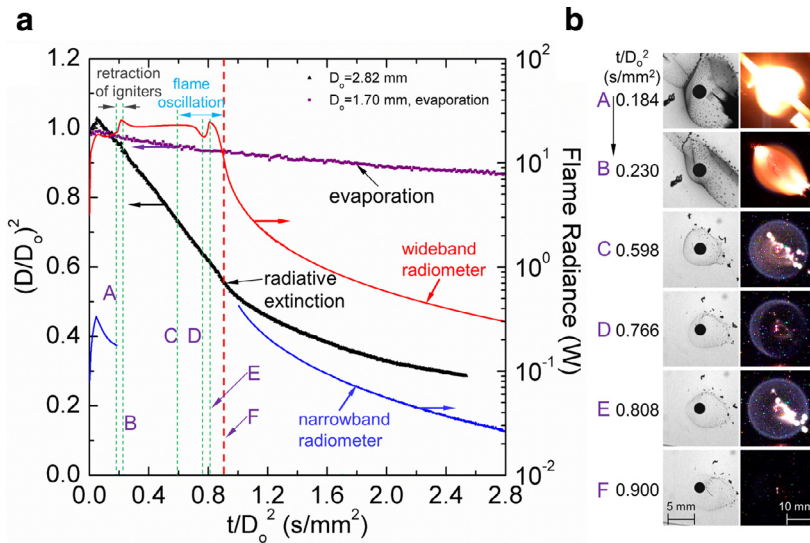


Fig. 5. (a) Evolution of droplet diameter and flame radiance for $D_o = 2.82$ mm; (b) selected images corresponding to the times (A, B, etc.) in ‘a’: A, onset of igniter retraction; B, end of igniter retraction; C, onset of flame open-up; D, flames opens to the maximum angle; E, end of flame close-back; F, disappearance of the visible flame. Color photos C, D, E in ‘b’ are contrast-enhanced to better show the flame.

correlations developed from data reported by Incropera and DeWitt [41].

Figure 3b shows that the predicted $T_{f,max}$ using Eq. (1) decreases with increasing D_o . The cooler flame places the flame closer to the droplet as expected so that D_f/D decreases which is consistent with Fig. 4. It is also evident from Fig. 3b that for $D_o < 1$ mm, $T_{f,max} \sim 2200$ K which is consistent with predicted T_f for sub-millimeter droplets [16,17]. With a large enough increase in D_o , T_f can conceivably drop below the soot inception temperature [42] so the flames of large droplets could show the characteristic dim blue color indicative of reduced sooting [43]. This trend confirms that with larger droplet size, radiative losses cool the flame.

The previously reported scaling [26] based on an energy balance for a control volume encompassing the flame shows that when radiation is a dominant energy loss mechanism, $K \sim D_o^{-n}$ where $n \approx 2/7$. The decreased $T_{f,max}$ in Fig. 3b with increasing D_o will lower K which is broadly consistent with the trends in Fig. 3a. For $D_o < 2$ mm, radiation is not dominant and this scaling does not apply to smaller drops. In particular, the GB data show little influence of D_o on K which is consistent with a negligible influence of radiation [22–24,44].

Figure 5 provides a closer examination of the extinction process for one particular droplet diameter ($D_o = 2.82$ mm). Included are measurements of wideband and narrowband radiative emissions. Note that the radiometer data are calibrated in such a way that radiation caused by the igniter coils is subtracted so that the data are representative of actual flame radiation. Since narrowband emissions

saturate the radiometer from 0.18 to 1.00 s/mm², there are no narrowband radiometer data in this range. The photographs in Fig. 5b correspond to the times indicated in Fig. 5a. The flame images in Fig. 5b are contrast-enhanced to better reveal the flame dynamics at extinction.

Before time ‘A’, the droplet is ignited but the coils are not yet retracted. From A to B the coils are retracted and radiative emissions increase and remain constant from B to C where wideband emissions are nearly constant. A point is reached where fuel flow to the droplet by evaporation cannot keep pace with radiative losses and the flame begins to extinguish. The images C, D, and E show the flame dynamics that result. The flame opens (D) then closes (E). Concurrently, the flame radiance shows evidence of oscillating.

The oscillatory flame motion (e.g., as noted in [26,45]) and evolution of droplet diameter shown in Fig. 5 is not thought to share the same mechanism as in previous studies where flame oscillations were predicted under certain conditions and identified with LTC regimes of burning. For example, simulations of *n*-decane droplet burning in an ambience of 600 to 1100 K [28] showed that the transition from high to low temperature burning was accompanied by an oscillating flame temperature. And, burning at elevated pressures was predicted to be accompanied by oscillating flames in some cases, though oscillations were not predicted for burning at atmospheric pressure [18]. An alternative explanation analyzed the complex oxygen transport to moving droplets and showed that only when droplets move in a regime where radiative

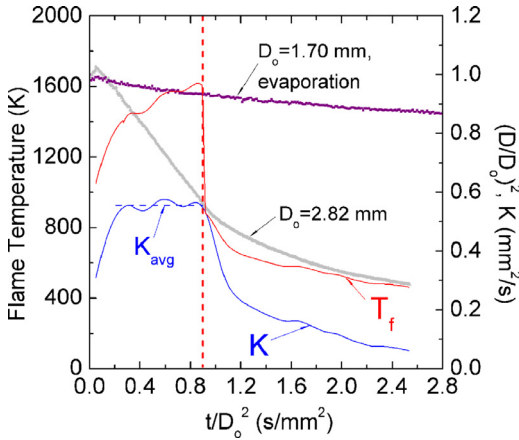


Fig. 6. Temporal evolution of computed flame temperature for $D_o = 2.82$ mm. K is obtained from taking derivatives of the D^2 data in Fig. 5a (reproduced here by the gray symbols). The vertical red dashed line indicates the time for radiative extinction (cf. Fig. 5a).

transport is important will flame oscillations occur for burning in the standard atmosphere: stationary droplet flames under such conditions will apparently not oscillate [46]. Such motion can be set up as an artifact of the droplet deployment process. In the present study, the flame in Fig. 5b appears more to ‘flicker’ than ‘oscillate’ as burning transitions to a post-extinction regime.

The data in Fig. 5a show that there is no abrupt change in narrowband emissions after visible flame extinction (time F), nor does K remain constant for a time in the post-radiative extinction regime as would be typical of a LTC regime of burning. Rather, K changes gradually and eventually reaches a value that is close to the pure evaporation limit. These trends [14,17,25–27, 30] point to the absence of a LTC regime of burning for *iso*-octane.

To explore the extent to which the post-visible flame extinction regime may exhibit LTC behavior, Eq. (1) is used to estimate T_f from the instantaneous K values obtained based on D^2 data shown in Fig. 5a. K is determined by taking derivatives based on two adjacent data points in the D^2 plot and the trend is processed by moving average and smooth functions in Matlab to reduce the noise and obtain a smooth curve of K . In the post-extinction regime where the flame is not visible after ~ 0.9 s/mm² (e.g., 2.91:1.2 in Fig. 1), we use the approximation that $D_f/D \approx 3.2$ in the LTC region [17,47]. The results are depicted in Fig. 6. K_{avg} marked by horizontal dashed line in Fig. 6 indicates the averaged K from the most linear portion of D^2 data prior to extinction. Here K_{avg} equals to 0.555 mm²/s which is consistent with the value presented in Fig. 3a for $D_o = 2.82$ mm.

The trends shown in Fig. 6 illustrate that in the region $t/D_o^2 < 0.9$ s/mm², predicted T_f are rather high and indicative of typical hot-flame combustion. The maximum T_f of ~ 1600 K in Fig. 6 is consistent with $T_{f,max}$ in Fig. 3b for $D_o = 2.82$ mm. However, the drop in K associated with flame extinction results in T_f decreasing to ~ 700 K at ~ 1.1 s/mm² and continues to drop in a rather monotonic regime. Even though the scale analysis results in Fig. 6 are consistent with detailed predictions of LTC burning for other fuels [27,47] that reported T_f similar to what is displayed in Fig. 6, such a trend is not especially indicative of entering an LTC burning regime [30] as an elevated temperature in the post-extinction regime is not sustained. Eventually the predicted T_f drops to values more typical of evaporation in a warm ambience (i.e., 426 K). Though the results discussed above are based on data for $D_o = 2.82$ mm, the trends are observed for all the large *iso*-octane droplets in the present study that exhibit extinction.

4. Conclusions

The burning histories of *iso*-octane droplets show a clear dependence on D_o with K decreasing as D_o increases. For $D_o > 2$ mm, an inverse power law correlates the measurements in the form $K \sim D_o^{-0.274}$ which is consistent with a scale analysis based on an energy balance on the flame. Droplets with $D_o \geq 2.7$ mm radiatively extinguish as shown by a significant drop of flame radiance and burning rates rather abruptly decrease to values approaching pure evaporation in the post-extinction burning regime. It is unclear if *iso*-octane droplets enter an LTC regime of burning in the post-radiative extinction regime because K and predicted T_f gradually decrease rather than remaining relatively constant in this regime. The FSR is found to decrease with increasing D_o for large droplets due to significant radiative losses and a predicted lowering of T_f . Furthermore, the SSR increases with increasing D_o , perhaps because of a weakened thermophoretic force as D_o increases though this trend is not fully understood.

Acknowledgments

This research was funded by the National Aeronautics and Space Administration under Grants NNX08AI51G. The authors thank D.L. Dietrich (NASA) and V. Nayagam (Case Western Reserve University) for some assistance with the ISS experiments. The help of Hee Dae Tak, Meilin Dong, Do Hyun Chung, Nan Wei, and Yiren Shen with some of the experiments and video image analysis is appreciated. We also appreciate the interest of F.A. Williams (UCSD), F.L. Dryer (Princeton), and T. Farouk (U South Carolina) in this study.

Supplementary materials

Supplementary material associated with this article can be found, in the online version, at doi:10.1016/j.proci.2016.07.096.

References

- [1] O. Gerbes, H.J. Hall, A.E. Becker, *Petrol. Process.* 2 (1947) 847–850.
- [2] H.M. Trimble, L.A. McReynolds, B. Mitacek, *Petrol. Process.* 3 (1948) 765–768.
- [3] Y.C. Liu, C.T. Avedisian, *Combust. Flame* 159 (2012) 770–783.
- [4] J.A. Widegren, T.J. Bruno, *Ind. Eng. Chem. Res.* 47 (2008) 4342–4348.
- [5] S. Dooley, S.H. Won, J. Heyne, et al., *Combust. Flame* 159 (2012) 1444–1466.
- [6] P.G. Aleiferis, J. Serras-Pereira, D. Richardson, *Fuel* 109 (2013) 256–278.
- [7] F. Contino, F. Foucher, P. Dagaut, T. Lucchini, G. D'Errico, C. Mounaim-Rousselle, *Combust. Flame* 160 (2013) 1476–1483.
- [8] T. Malewicki, A. Comandini, K. Brezinsky, *Proc. Combust. Inst.* 34 (2013) 353–360.
- [9] S. Tanaka, F. Ayala, J.C. Keck, J.B. Heywood, *Combust. Flame* 132 (2003) 219–239.
- [10] H.J. Curran, W.J. Pitz, C.K. Westbrook, G.V. Callahan, F.L. Dryer, *Proc. Combust. Inst.* 27 (1998) 379–387.
- [11] P. Dagaut, M. Reuillon, M. Cathonnet, *Combust. Sci. Technol.* 95 (1993) 233–260.
- [12] H.J. Curran, P. Gaffuri, W.J. Pitz, C.K. Westbrook, *Combust. Flame* 129 (2002) 253–280.
- [13] W.A. Sirignano, *Fluid Dynamics and Transport of Droplets and Sprays*, Cambridge University Press, Cambridge, UK, 1999, pp. 10–21.
- [14] A. Cuoci, M. Mehl, G. Buzzi-Ferraris, T. Faravelli, D. Manca, E. Ranzi, *Combust. Flame* 143 (2005) 211–226.
- [15] T.I. Farouk, Y.C. Liu, A.J. Savas, C.T. Avedisian, F.L. Dryer, *Proc. Combust. Inst.* 34 (2013) 1609–1616.
- [16] Y.C. Liu, T. Farouk, A.J. Savas, F.L. Dryer, C.T. Avedisian, *Combust. Flame* 160 (2013) 641–655.
- [17] T.I. Farouk, F.L. Dryer, *Combust. Flame* 161 (2014) 565–581.
- [18] T.I. Farouk, M.C. Hicks, F.L. Dryer, *Proc. Combust. Inst.* 35 (2015) 1701–1708.
- [19] G.M. Faeth, D.R. Olson, in: SAE International Paper # 680465, 1968.
- [20] C.T. Avedisian, G.S. Jackson, *J. Propul. Power* 16 (2000) 974–979.
- [21] Y.C. Liu, Y. Xu, C.T. Avedisian, M.C. Hicks, *Proc. Combust. Inst.* 35 (2015) 1709–1716.
- [22] A.J. Marchese, F.L. Dryer, *Combust. Sci. Technol.* 124 (1997) 371–402.
- [23] A.J. Marchese, F.L. Dryer, R.O. Colantonio, *Proc. Combust. Inst.* 27 (1998) 2627–2634.
- [24] V. Nayagam, A. Marchese, K. Sacksteder, in: K. Saito (Ed.), *Progress in Scale Modeling*, Springer, Netherlands, 2008, pp. 169–178.
- [25] V. Nayagam, D.L. Dietrich, P.V. Ferkul, M.C. Hicks, F.A. Williams, *Combust. Flame* 159 (2012) 3583–3588.
- [26] Y.C. Liu, Y. Xu, M.C. Hicks, C.T. Avedisian, *Combust. Flame* 171 (2016) 27–41.
- [27] V. Nayagam, D.L. Dietrich, M.C. Hicks, F.A. Williams, *Combust. Flame* 162 (2015) 2140–2147.
- [28] A. Cuoci, A. Frassoldati, T. Faravelli, E. Ranzi, *Proc. Combust. Inst.* 35 (2015) 1621–1627.
- [29] C.T. Avedisian, B.J. Callahan, *Proc. Combust. Inst.* 28 (2000) 991–997.
- [30] D.L. Dietrich, V. Nayagam, M.C. Hicks, et al., *Microgravity Sci. Technol.* 26 (2014) 65–76.
- [31] B. Banu, Fluids and combustion facility (FCF) and combustion integrated rack (CIR), in: NASA John H. Glenn Research Center (Ed.), *Payload Accommodations Handbook*, Cleveland, Ohio, 2008 CIR–DOC-4064.
- [32] J. Robbins, C. Shinn, *Multi-user droplet combustion apparatus flex2*, in: NASA John H. Glenn Research Center (Ed.), Cleveland, Ohio, 2010.
- [33] CRC Handbook of Chemistry & Physics, Taylor and Francis Group, LLC., 2014–2015, pp. 3–536, 5–68, 6–145.
- [34] Propulsion Chemistry Division, *Basic Considerations in the Combustion of Hydrocarbon Fuels with Air*, in: H.C. Barnett, R.R. Hibbard (Eds.), Lewis Flight Propulsion Laboratory, Washington D.C., 1959 (<http://ntrs.nasa.gov/archive/nasa/casi.ntrs.nasa.gov/19930091007.pdf>).
- [35] C.L. Dembia, Y.C. Liu, C.T. Avedisian, *Image Anal. Stereol.* 31 (2012) 137–148.
- [36] S.H. Chung, C.K. Law, *Combust. Flame* 64 (1986) 237–241.
- [37] G.S. Jackson, C.T. Avedisian, J.C. Yang, *Int. J. Heat Mass Transfer* 35 (1992) 2017–2033.
- [38] S.R. Turns, *An Introduction to Combustion*, McGraw-Hill, New York, 2012, pp. 374–396.
- [39] C.K. Law, F.A. Williams, *Combust. Flame* 19 (1972) 393–405.
- [40] R.C. Reid, J.M. Prausnitz, B.E. Poling, *The Properties of Gases and Liquids*, McGraw-Hill, New York, 1987, pp. 498–504.
- [41] F.P. Incropera, D.P. DeWitt, *Introduction to Heat Transfer*, Wiley, New York, 2002, p. 831.
- [42] R.A. Dobbins, *Combust. Flame* 130 (2002) 204–214.
- [43] D.L. Dietrich, J.B. Haggard Jr, F.L. Dryer, V. Nayagam, B.D. Shaw, F.A. Williams, *Proc. Combust. Inst.* 26 (1996) 1201–1207.
- [44] G.S. Jackson, C.T. Avedisian, *Combust. Sci. Technol.* 115 (1996) 125–149.
- [45] V. Jaggard Zero-G fire pulses like a jellyfish on the space station. August 22, 2014. (<http://www.smithsonianmag.com/science-nature/zero-g-fire-pulses-jellyfish-space-station-180952454/?no-ist>).
- [46] F. Takahashi, V.R. Katta, M.C. Hicks, Local extinction and oscillations of n-heptane envelope diffusion flames in microgravity, *31st Annual Meeting of the American Society for Gravitational and Space Research*, Alexandria, Virginia, 2015, November 11–14.
- [47] V. Nayagam, D.L. Dietrich, F.A. Williams, *AIAA J.* 54 (2016) 1235–1239.